
PAPER

Soft landing of runaway currents by ohmic field in J-TEXT tokamak

To cite this article: Jie HU *et al* 2020 *Plasma Sci. Technol.* **22** 115102

View the [article online](#) for updates and enhancements.

Soft landing of runaway currents by ohmic field in J-TEXT tokamak

Jie HU (胡捷)¹, Wei YAN (严伟)^{1,5}, Ruihai TONG (佟瑞海)^{1,2,5}, Wei LI (李维)¹, Zhongyong CHEN (陈忠勇)^{1,3}, Anjue DAI (戴岸珏)¹, Duwei HUANG (黄都伟)⁴, Yunong WEI (魏禹农)¹, Tiankui MA (马天逵)¹, Yuan HUANG (黄缘)¹, Yang LI (李阳)¹, Wei ZHENG (郑玮)¹, Zhifang LIN (林志芳)¹, You LI (李由)¹, Huaiyu YANG (杨怀玉)¹, Duoqin WANG (王铎钦)¹, Wei BAI (白炜)¹, Yu ZHONG (钟昱)¹, Jiangan FANG (方建港)¹ and J-TEXT Team^{1,6}

¹International Joint Research Laboratory of Magnetic Confinement Fusion and Plasma Physics, State Key Laboratory of Advanced Electromagnetic Engineering and Technology, School of Electrical and Electronic Engineering, Huazhong University of Science and Technology, Wuhan 430074, People's Republic of China

²Southwestern Institute of Physics, Chengdu 610041, People's Republic of China

³Chengdu University, Chengdu 610106, People's Republic of China

⁴Beibu Gulf University, Qinzhou 535000, People's Republic of China

E-mail: yanwei1090@hust.edu.cn and tongruihai@gmail.com

Received 12 May 2020, revised 14 July 2020

Accepted for publication 15 July 2020

Published 10 September 2020



CrossMark

Abstract

Recently, experimental studies on the soft landing of RE current by ohmic (OH) field have been performed in J-TEXT tokamak, as a possible auxiliary method to dissipate the RE current. With optimized horizontal displacement control of the RE beam, the toroidal electric field has been scanned from 1.6 to -0.3 V m^{-1} during the RE plateau phase. The growth rate of RE currents and the evolution of hard x-ray (HXR) emissions have been studied. It is found that when the toroidal electric field is less than 7–12 times the theoretical critical electric field, the decay of REs could be achieved. The dissipation rate by the ohmic field can reach a maximum value of 3 MA s^{-1} . Furthermore, the results of HXR spectra analysis indicate the different behaviors of HXR emissions under the condition of different toroidal electric fields. The analysis of the ionized argon emissions and magnetic fluctuations shows that under the condition of different toroidal electric fields, the physical process of RE generation may be different.

Keywords: tokamak, disruption, runaway electron, hard x-ray

(Some figures may appear in colour only in the online journal)

1. Introduction

Due to the large toroidal electric field during the current quench (CQ) of disruptions, it is predicted that a large runaway electron (RE) current could be generated in ITER [1–3]. REs with several tens of mega-electron volt (MeV) energy striking the plasma facing components (PFCs) will threaten the safe operation of tokamaks. In order to achieve collisional suppression of the REs generated during disruptions, massive gas injection (MGI) [4–9] and shattered pellet injection (SPI)

[10, 11] system have been established in many devices. But the high- Z impurities injected cannot increase the electron density enough to reach the Rosenbluth–Putvinski density [12], which is related to the theoretical critical electric field.

Furthermore, the application of resonant magnetic perturbations (RMPs) can significantly reduce the RE current in ASDEX Upgrade [13] and COMPASS [14]. Even in some devices [15–17], the RE current can be significantly suppressed by RMP. However, for the large device JET, the RMP has failed to suppress the RE generation during disruptions [18]. Results of experiments and simulations in DIII-D have shown that MHD instabilities may be effective in the RE current mitigation [19, 20]. Excitation of whistler and

⁵ Authors to whom any correspondence should be addressed.

⁶ See Liang *et al* (<https://doi.org/10.1088/1741-4326/ab0745>) for the J-TEXT Team.

Alfvénic waves by REs observed in the series of experiments in DIII-D [21–24] can cause an increase of RE loss. Accordingly, it is possible to develop a novel method for RE current mitigation based on these studies of instabilities.

Once the suppression of REs failed, the RE current will be formed. The RE current with huge magnetic energy and kinetic energy must be dissipated or soft landed to reduce the damage to the device. The dissipation of RE current by high-Z MGI has been performed in several devices, while the dissipation effect becomes saturated with the increase of injected impurity quantity [25, 26]. Post-disruption RE beam dissipation by the SPI in DIII-D has been reported, but the dissipation effect does not show a significant difference between pellets and gas [27]. An alternative method is to ramp down RE current plateau by reducing the toroidal electric field, i.e. the soft landing of RE current.

The theory in [12] has shown that the avalanche growth is predicted to not occur when the toroidal electric field of post-disruption plasma is less than the theoretical critical electric field, i.e. $E/E_{\text{crit}} < 1$. Whether for suppression, dissipation or soft landing, it is particularly important to determine the critical electric field $E_{\text{crit}} = \varepsilon^3 n_{e,\text{tot}} \ln \Lambda (Z) / (4\pi \varepsilon_0^2 m_e c^2)$, which is a function of the total (free or bound) electron density $n_{e,\text{tot}}$. It indicates that the toroidal electric field and total electron density together determine the value of E/E_{crit} . Experimental measurements of RE growth and decay rates under quiescent conditions have been performed in DIII-D, and the transition of HXR emissions from growth to decay has been found to occur 3–5 times above the theoretical critical electric field for avalanche growth [28]. Later, a variety of ITPA joint experiments in many devices (including DIII-D, C-Mod, FTU, KSTAR, and TEXTOR) have measured the RE generation threshold electric field based on observations of RE onsets during the flattop phases, which is related to Dreicer generation. The measured threshold electric field on these devices of joint experiments is in the range of 4.5–12 times above E_{crit} [29]. Simulations considering the whistler wave instability have indicated that the excitation of whistler waves can increase the critical electric field and produced a threshold of $E/E_{\text{crit}} \sim 6.4$, which is much closer to the above observations [30]. The growth/decay rate of plateau-phase RE currents with applied positive/negative toroidal electric field has also been measured in DIII-D. It has been found that the RE current transition from growth to decay is at $E - E_{\text{crit}} \approx 1.0 \text{ V m}^{-1}$, and a fairly constant anomalous dissipation rate of order 10 s^{-1} exists [31].

Most of the experimental data on the RE generation threshold electric field come from the non-disruptive discharges, while the motivation for the above studies is REs during disruptions. Therefore, in order to obtain more data of disruptive discharges, the soft landing of RE currents by ohmic field is performed in J-TEXT, scanning the surface toroidal electric field from 1.6 to -0.3 V m^{-1} during RE plateau phases. After the position of RE beam has been well controlled, the significant ramp down of RE currents can be observed when the surface toroidal electric field is less than about 0.6 V m^{-1} in J-TEXT. The RE current growth/decay rate and HXR emission growth/decay rate are both measured to describe the RE growth rate and compared with the

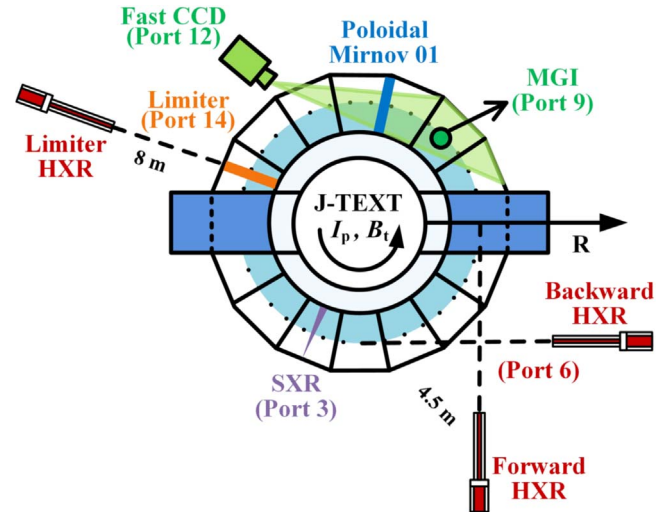


Figure 1. The top view with the toroidal locations of the main diagnostics and MGI valves in J-TEXT tokamak. The distances from the Forward HXR detector and the Backward HXR detector to the chamber wall are 4.5 m. The distance from the Limiter HXR detector to the limiter is 8 m.

avalanche theory. In addition, when the different toroidal electric fields are applied, the evolution of HXR emissions is analyzed in detail to study the RE loss characteristics.

This paper is organized as follows. In section 2, the experimental setup in J-TEXT is presented. In section 3, the typical experimental results are described, including the soft landing of RE current by the applied toroidal electric field and the measurement of RE current growth rate in J-TEXT. In section 4, the analysis of HXR bremsstrahlung spectra during disruptions is presented. The discussion is given in sections 5 and 6 is the summary.

2. Experimental setup

2.1. Experimental scenario

The experiments mentioned in this paper are performed in limiter configuration discharges in J-TEXT tokamak, which is a conventional iron core tokamak, operated at the major radius $R = 1.05 \text{ m}$, the minor radius $a = 0.25\text{--}0.29 \text{ m}$ with a movable titanium-carbide-coated graphite limiter [32]. Typical pre-disruption plasma parameters are plasma current $I_p = 120\text{--}150 \text{ kA}$, toroidal magnetic field $B_T = 2 \text{ T}$ (and edge safety factor $q_a = 4.1\text{--}5.2$ respectively). The line averaged electron density is in the range of $n_e \sim (1\text{--}2) \times 10^{19} \text{ m}^{-3}$ and the electron temperature $T_e \sim 0.8 \text{ keV}$. Under the above pre-disruption plasma parameters, the runaway (RE) current can be stably generated with MGI injection (about 2×10^{20} argon atoms) in J-TEXT tokamak [33].

2.2. Key diagnostics

Figure 1 shows the top view with the toroidal locations of the main diagnostics during disruptions and MGI valves in J-TEXT.

To study the REs during the flattop and the RE current plateau phase, the hard x-ray (HXR) spectrometer system has been developed in J-TEXT tokamak. The spectrometer system contains several NaI scintillator detectors and a multi-channel analyzer (MCA) with 0.5 ms time resolution and 512 channels energy resolution [34]. These scintillator detectors are used to measure the HXR emissions in the energy range of 0.4–10 MeV resulting from the thick target bremsstrahlung when REs are lost from the plasma and impact on the vessel walls [35–37]. However, the measurements of the HXR emissions during the RE plateau regime are much more challenging because HXR emissions could reach the rates of 10^5 – 10^6 counts s^{-1} and higher. In order to prevent the output signals of detectors from saturating, the lead bricks have been placed in front of these detectors to shield part of HXR emissions. The HXR detector towards the limiter is still saturated due to a large amount of HXR emissions during disruptions.

Two HXR detectors are distributed in the forward and the backward REs movement direction to measure small pitch-angle (less than 90°) and large pitch-angle (more than 90°) lost REs, respectively. In the following, ‘Forward HXR’ and ‘Backward HXR’ are used to represent these two HXR detectors. The positions of the Forward HXR detector and the Backward HXR detector are at the mid-plane with 4.5 m away from the chamber wall, and the collimation ports are aligned with the centerline of the vacuum vessel.

In addition, a fast frame visible camera which points at the MGI with a proper optical filter is used to monitor the penetration of impurity gas jet. Photos from the fast frame visible camera are filtered by Ar II (442.6 nm) filter for gas argon.

2.3. RE beam displacement control

In the event of failure of RE suppression, control of RE current and soft landing or dissipation of it are essential. During the thermal quench (TQ), the rapid drop in internal inductance means that the plasma is no longer in radial force equilibrium. However, the vertical field (VF) system maintaining radial equilibrium is essentially constant on the sub-millisecond timescale of TQ [38]. Without optimized horizontal displacement control, the RE beam in J-TEXT will drift toward the low field side under the action of centrifugal force.

Experimental studies on the control of post-disruption RE beam have been documented in many devices, including TFTR, FTU, TCV, DIII-D and COMPASS [38–42]. Referring to the control strategies in the above devices, similar experiments have been carried out by modifying the initial reference displacement of the VF. This strategy can avoid horizontal drift of RE beams toward the low field side, maintaining the RE beams in a safe position within the vacuum vessel, and avoiding the rapid termination of RE current. Without optimized horizontal displacement control (i.e. modifying the initial reference displacement of VF), the RE plateau is only lasting less than 20 ms. After the

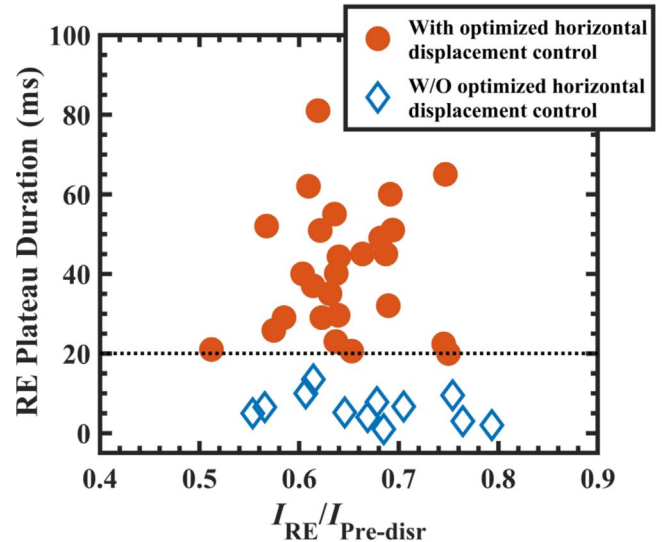


Figure 2. RE plateau duration versus the ratio of RE current I_{RE} and pre-disruption plasma current $I_{Pre-disr}$. Orange circles represent discharges with optimized horizontal displacement control. Blue rhombuses represent discharges without optimized horizontal displacement control. Each point represents one discharge.

displacement control has been optimized, the RE plateau could be significantly elongated to more than 80 ms, as the statistical result illustrated in figure 2. Precise control of the VF could significantly lengthen the duration of RE plateau and provide preparation for following RE current soft landing experiments.

3. Experimental results

3.1. Soft landing of runaway current

Under the stable control of the RE beam position, externally applied positive and negative toroidal loop voltages have a significant effect on the decay rate of RE current. In J-TEXT, rectification angle α of ohmic field coils could be modified to adjust the output voltage and the output power of OH field coils. The system of OH field coils is a 12-pulse rectifier bridge and its output voltage $V_{OH} = 2.34E \cos \alpha$, where E is the secondary side voltage of the rectifier transformer ($E = 145$ V), and the adjustable range of rectification angle α is 20° – 160° . Because there is ohmic heat only, in the general discharge without external toroidal electric field applied, the role of the OH field is to maintain the plasma current and constantly provide energy for the RE beam. It is feasible to control the toroidal loop voltage V_{loop} as well as the toroidal electric field by modifying the OH field output voltage V_{OH} during the RE plateau phase.

Time traces of plasma parameters from three discharges differing primarily in the externally applied toroidal loop voltage during disruptions are shown in figure 3. The external toroidal loop voltage is applied at the beginning of RE plateau phase on purpose, and the OH field output voltage reaches the set value at 0.31 s. In the general discharge (without

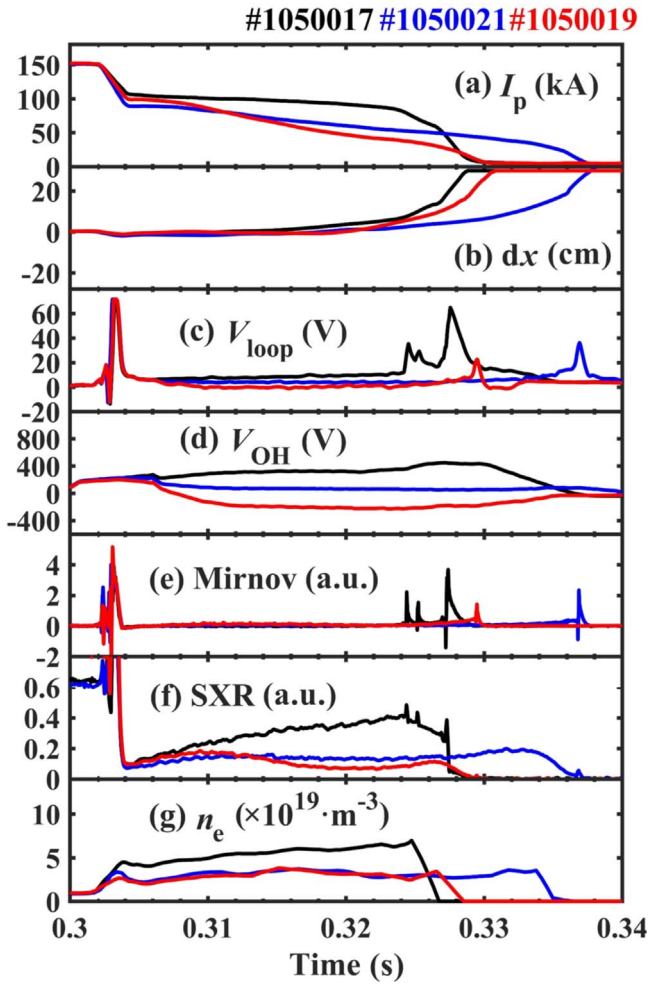


Figure 3. Time traces from three discharges showing (a) plasma current I_p , (b) horizontal position of the plasma dx , (c) toroidal loop voltage V_{loop} , (d) ohmic field voltage V_{OH} , (e) Mirnov signal, (f) soft x-ray signal, (g) central line-averaged electron density n_e . For the general discharge #1050017 represented by black curves, its average toroidal loop voltage $V_{loop} \sim 10$ V during the RE plateau phase. For the discharges #1050021 and #1050019 with externally applied toroidal loop voltage represented by blue and red curves, their average toroidal loop voltages $V_{loop} \sim 5$ V and $V_{loop} \sim 0$ V during the RE plateau phase. The evolution trend of each signal in the discharge whose toroidal loop voltage is adjusted to the maximum (not shown in this figure) is almost the same with the general discharge #1050017.

modifying OH field voltage) with average toroidal loop voltage V_{loop} is about 10 V (black curve, shot #1050017 in figure 3), the decay rate of RE current is very small. The average OH field voltage V_{OH} is about 327 V. Mirnov signal shows that strong magnetic magnetohydrodynamic (MHD) activities have appeared in the CQ and the termination of RE current. The SXR emissions rapidly decline in CQ, and then gradually increase during the RE plateau phase. In the termination of RE current, the SXR emissions reach the maximum value and immediately drop down to zero. Each SXR emission spike corresponds to each burst of toroidal loop voltage and the Mirnov signal. Line averaged electron density is slowly rising with slight fluctuation.

As for the discharge whose toroidal loop voltage is adjusted to the maximum (not shown in figure 3), the evolution trend of each signal is almost the same with the general discharge #1050017 (i.e. the discharge without external toroidal loop voltage applied). It can be considered that the output voltage of the OH field remains at the maximum value within the adjustable range in the general discharge.

Then for the discharge whose average toroidal loop voltage V_{loop} is about 5 V (blue curve, shot #1050021 in figure 3), significant ramping down of RE current could be seen in figure 3. The average value of OH field voltage V_{OH} decreases to about 58 V. From the beginning of RE plateau to 0.31 s, SXR emissions rise slightly and then remain unchanged. During the termination of RE current, SXR emissions increase slightly again. Compared to the general discharge, the level of SXR emissions drops a lot. Line averaged electron density remains unchanged in the RE plateau phase. Both in toroidal loop voltage and Mirnov signal, only a small spike appears in the final loss phase.

For the discharge whose average toroidal loop voltage V_{loop} is about 0 V and average OH field voltage V_{OH} is about -216 V (red curve, shot #1050019 in figure 3), the decay rate of RE current is larger than that of shot #1050021. Spikes of toroidal loop voltage and Mirnov signal are also smaller. During the soft-landing phase, SXR emissions have a significant decline. So, the soft landing of RE current has been achieved by controlling the toroidal electric field reduction.

3.2. Runaway current growth rate

Previous work of theory for REs avalanche in [12] and DIII-D [31] has shown that due to the knock-on avalanche mechanism, the growth rate of RE current density $\nu_R = J_R^{-1} dJ_R/dt$ is given approximately by

$$\nu_R = \frac{eE_{crit}}{(1 + \alpha_R)m_e c \bar{p}} (E_{sur}/E_{crit} - 1), \quad (1)$$

where $\alpha_R \equiv I_R l_i / (\bar{p} I_A)$, and l_i is the plasma dimensionless self-inductance, $\bar{p} = [3(Z + 5)/\pi]^{1/2} \ln \Lambda(Z)$ is the mean value of p predicted for avalanching REs, $\ln \Lambda$ is the Coulomb logarithm, $I_A = 4\pi m_e c / (\mu_0 e) = 17$ kA is the Alfvén current. E_{sur} is surface field, $E_{crit} = e^3 n_{e,tot} \ln \Lambda(Z) / (4\pi \epsilon_0^2 m_e c^2) = 0.0051 n_{e20} \ln \Lambda(Z)$ is the equivalent ‘critical field’ associated with the minimum collisional drag force (or stopping power) experienced by a fast electron passing through a medium of atomic number Z and total (free or bound) electron density $n_{e,tot}$. It can be seen that $(E_{sur}/E_{crit} - 1) \propto J_R^{-1} dJ_R/dt$.

One important issue is to estimate the value of the plasma internal inductance l_i . The soft x-ray emission profile can be used to roughly estimate the l_i . The approximate l_i is given by [43]:

$$l_i = \frac{1}{2} + 2 \ln[a / (\Delta Z_{curr} / 2)], \quad (2)$$

where a is the minor radius of the plasma, and the width of the runaway current profile ΔZ_{curr} has been characterized by the full width of the soft x-ray emission profile peak at $1/e$ of its maximum. Through this method, the internal inductance l_i is about 1.3 in J-TEXT tokamak [44].

Another more important issue for the next-generation device is to confirm the value of ‘critical field’ E_{crit} for RE generation. The total electron density is difficult to obtain due to the lack of suitable diagnostics in J-TEXT, such as spectroscopy diagnostic or neutral pressure measurement on the vacuum vessel. Here we take a rough method to estimate the total electron density. After impurity injection by MGI, the electron density will increase due to the partial ionization of argon impurities. The change of the line-average electron density caused by the impurity can be expressed as $\Delta n_e = Z_{\text{mean}} n_{\text{imp}}$, where n_{imp} is the impurity density and Z_{mean} is the mean ionization state of the impurity [26]. The mean ionization state Z_{mean} is strongly dependent on the electron temperature but weakly dependent on the electron density. However, it is unavailable to measure the absolute electron temperature measurement T_e during disruptions in J-TEXT.

A method is adopted to estimate the post-TQ temperature T_e [45], where the exponential time constant of the current decay during CQ is a function of the electron temperature T_e . The decay of the plasma current during the CQ can be described with a simple circuit equation:

$$-L_p \frac{dI_p}{dt} \approx R_p I_p, \quad (3)$$

where the plasma is assumed to be a conductor of self-inductance L_p , with resistivity R_p . The currents in the OH coils cannot significantly change during a fast CQ and therefore they have little influence on the current decay. For L_p/R_p constant in time, the exponential time constant τ_{CQ} is

$$-\frac{dI_p}{dt} \frac{1}{I_p} = \frac{R_p}{L_p} = \tau_{\text{CQ}}^{-1}. \quad (4)$$

The total plasma inductance L_p can be approximated by

$$L_p = \mu_0 R_0 (\ln(8R_0/a) - 2 + l_i/2), \quad (5)$$

where μ_0 is the permeability of vacuum, a is the minor radius of the plasma, and R_0 is the major radius of the plasma. The plasma resistivity is

$$R_p = \frac{2\pi R_0 \rho}{S}, \quad (6)$$

where S is the plasma cross-section area. In consideration of impurity ions, the Spitzer resistivity can be expressed as [46, 47]:

$$\rho = Z_{\text{eff}} \frac{0.51 m_e^{1/2} e^2 \ln \Lambda}{3 \varepsilon_0^2 (2\pi T_e)^{3/2}}, \quad (7)$$

where the Coulomb logarithm $\ln \Lambda = 9$, and the effective Z is defined by

$$Z_{\text{eff}} = \frac{\sum_j n_j Z_j^2}{\sum_j n_j Z_j} = \frac{\sum_j n_j Z_j^2}{n_e}, \quad (8)$$

where Z_j is the impurity ion charge number and n_j is the ion density. The exponential time constant of the current decay

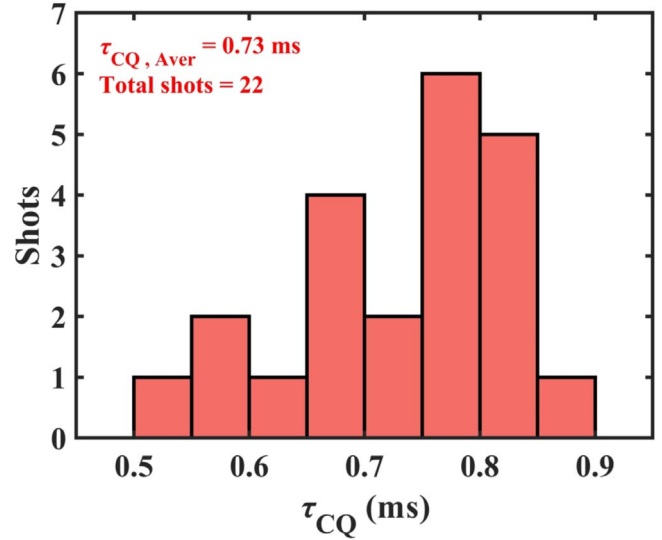


Figure 4. The statistics of current quench time constant τ_{CQ} for 22 discharges.

during CQ is

$$\tau_{\text{CQ}} = \frac{L_p S}{2\pi R_0 \rho}. \quad (9)$$

A linear decay rate is often as good as the exponential decay rate in describing the decay of the current between 80% and 20% I_p , so that the time constant τ_{CQ} can be defined as

$$\tau_{\text{CQ}} = \Delta t_{80-20} / \ln 4 = 0.72 \Delta t_{80-20} = 2.16 \Delta t_{90-70}, \quad (10)$$

where due to the formation of RE plateau, the current decay to about 60% I_p during the CQ phase. The decay of the current between 90% and 70% I_p has been selected to calculate the τ_{CQ} . Figure 4 gives the statistics of τ_{CQ} for 22 discharges. It can be found that τ_{CQ} is in the range of 0.5–0.9 ms and the average value is about 0.73 ms. Using this method, τ_{CQ} can be calculated knowing the electron temperature T_e . Then the Z_{mean} can be calculated by T_e . However, one issue must be noted: the Z_{eff} in equation (7) is related to the Z_{mean} (i.e. related to the ion composition of plasma). Therefore, at first, assume $Z_{\text{eff}} = 1$. After Z_{mean} is obtained through the above calculation, a new Z_{eff} can be obtained and used for the second iteration. After four iterations, the calculation error is less than 10^{-4} . The result of the fourth iteration is shown in figure 5, where $Z_{\text{eff}} = 1.45$. As shown in figure 5(a), the post-disruption electron temperature T_e is estimated as 2.58–3.62 eV, and the average value is 3.20 eV. The Z_{mean} calculated by T_e for argon based on the ionization-recombination equilibrium is shown in figure 5(b) with $n_e \sim (1 - 10) \times 10^{19} \text{ m}^{-3}$ during disruptions in J-TEXT. It can be clearly seen that Z_{mean} of the argon impurity is estimated to be in the range of 1.75–2.06 and the average value is 2.00.

Although the PFC material is graphite in J-TEXT, previous research has shown that the C^+ content is less than 5% and mainly concentrated at the plasma boundary during the flattop phase in J-TEXT [48]. For simple analysis, assume that the carbon composition can be neglected. In future work, the RE plasma composition during disruptions will be further

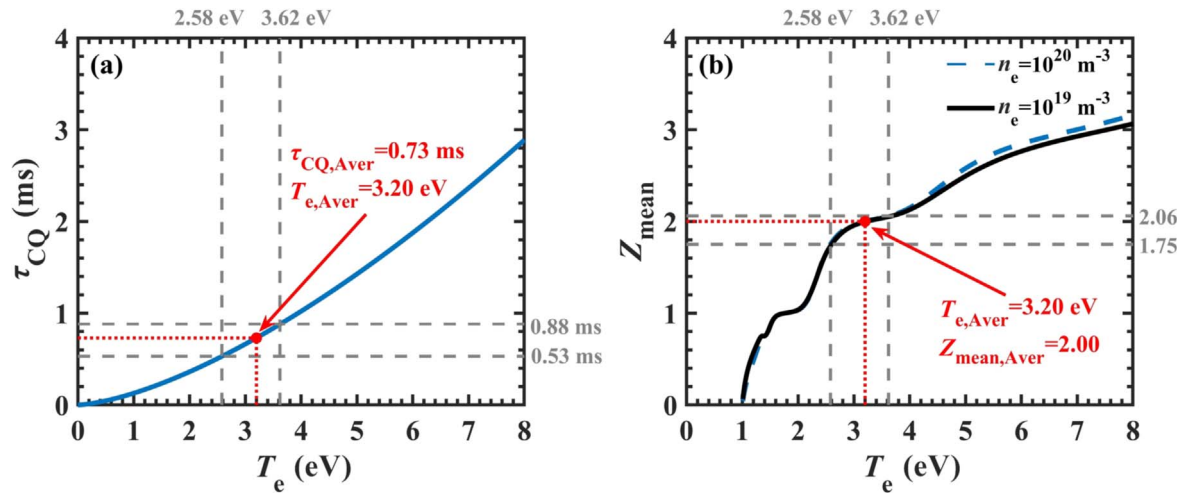


Figure 5. (a) The time constant of the current quench τ_{CQ} as a function of the electron temperature T_e . The red dotted lines represent the post-disruption $T_e \sim 3.20$ eV calculated with the average $\tau_{CQ} \sim 0.73$ ms. The gray dashed lines give the error bar based on the statistics of τ_{CQ} . (b) The mean ion charge Z_{mean} as a function of the electron temperature T_e . The black solid line represents the case of $n_e = 1 \times 10^{19} \text{ m}^{-3}$ and the blue dashed line represents the case of $n_e = 1 \times 10^{20} \text{ m}^{-3}$. The red dotted lines show the average $Z_{mean} \sim 2.00$ with average $T_e \sim 3.20$ eV. The gray dashed lines give the error bar of Z_{mean} .

measured accurately. Here, due to the $Z_{mean} \sim 2.00$, the argon ion density can be estimated as $n_{Ar^{2+}} \approx n_{imp} = \Delta n_e / Z_{mean}$. It is assumed that when C^+ content is ignored, the ionic composition during the RE plateau phase is 60%–81% H^+ mixed with 19%–40% Ar^{2+} through this rough estimate.

For bound argon electrons, the Coulomb logarithm is $\ln \Lambda = 9.932$ and for unbound (free) plasma electrons $\ln \Lambda = 19.2$. \bar{p} is only weakly dependent on Z . $\bar{p} = 46.5$ for drag on REs due to electrons bound to argon ($Z = 18$) and $\bar{p} = 46.3$ for drag due to free electrons [31], and the \bar{p} can be simply estimated as 46.4, for which only argon and free electrons are considered.

To study the RE current growth rate, the surface electric field E_{sur} has been scanned from 1.6 to -0.3 V m^{-1} during the RE plateau phase in J-TEXT, and the critical electric field is estimated as $E_{crit} \approx 0.04\text{--}0.24 \text{ V m}^{-1}$. The measured (blue squares) and predicted (red circles) RE current growth rate ν_R as a function of the ratio between surface electric field and the critical electric field, i.e. E_{sur}/E_{crit} , are shown in figure 6. The analysis method has been applied in DIII-D [31]. Each circle or square pair corresponds to the middle of the RE plateau in a single discharge when the plasma position and electron density vary relatively slowly. The horizontal error bars on the squares in figure 6 reflect the range in E_{crit} obtained from the error bar of Z_{mean} . When ignoring the scatter of the data, there is an obvious linear relation between the RE current growth rate and the surface field E_{sur} . The significant ramp down of RE currents can be observed when the surface toroidal electric field is less than about 0.6 V m^{-1} . The maximum ramp-down rate driven by the negative toroidal electric field is about 3 MA s^{-1} , which is much lower than by MGI with 28 MA s^{-1} in J-TEXT. The dissipation RE current by MGI injects a large amount of high- Z impurity gas, which may cause load on the vacuum vessel. Although the dissipation rate driven by the negative toroidal electric field is not as good as MGI, it still can be used as an auxiliary to

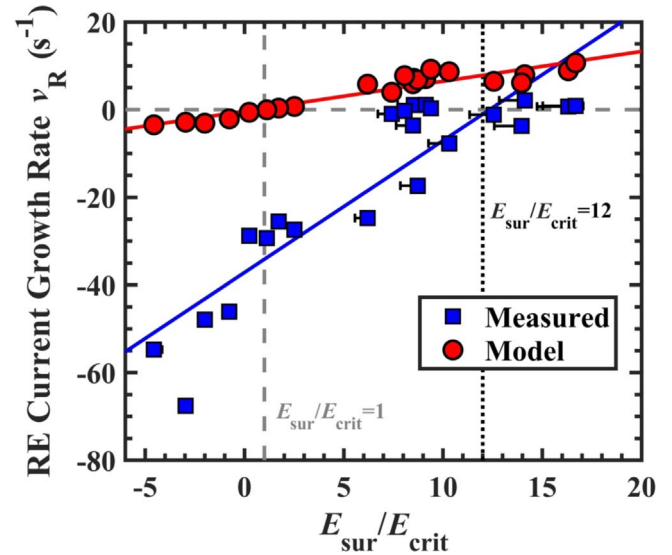


Figure 6. Measured (blue squares) and predicted (red circles) RE current growth rate ν_R as a function of surface electric field ratio critical electric field E_{sur}/E_{crit} . The data are from the 22 discharges which are shown in figure 4. Two straight solid lines are fitting lines of two sets of data.

MGI. When a certain dissipation rate of RE current is reached, combining these two strategies may require less gas injection, thereby reducing the requirements of MGI gas injection.

There are some differences between the trend of the experimental and theoretical curves. The intersection of the fitting line of measured points (blue line) and the horizontal axis is not at the point of E_{crit} in theory but the point of $\sim 12 \times E_{crit}$. When $E_{sur}/E_{crit} \sim -3$, the decay rate of RE current reaches its maximum of nearly 70/s. As for the intersection of the fitting line of measured points with $E_{sur}/E_{crit} = 1$, there is an anomalous RE current dissipation

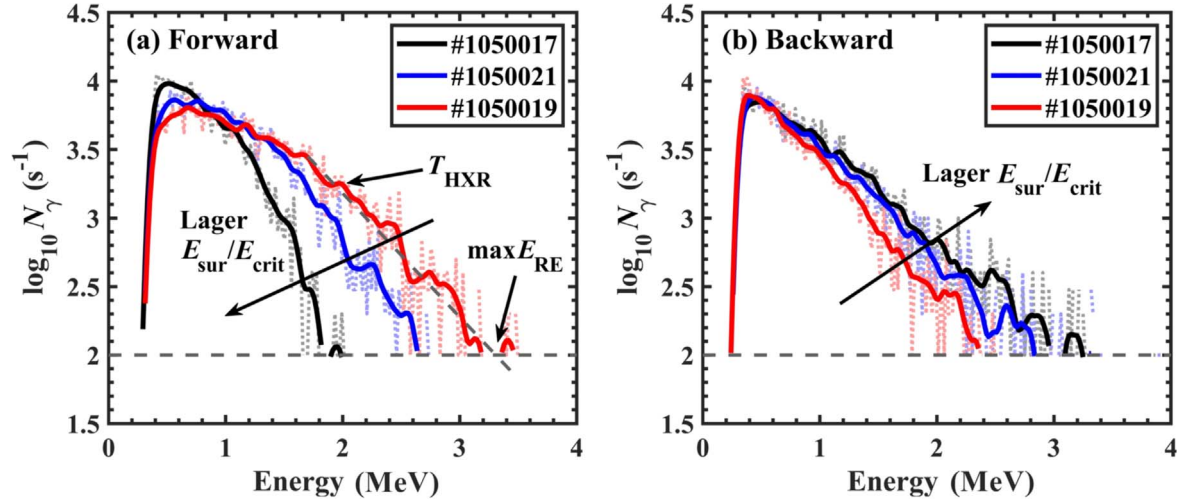


Figure 7. HXR bremsstrahlung spectra during the RE plateau phase from the Forward HXR detector (a) and from the Backward HXR detector (b), respectively. Two characteristic parameters $\max E_{RE}$ and T_{HXR} have been defined in (a). Curves are obtained after smoothed. The externally applied toroidal electric field during the RE plateau phase is different for three discharges. The E_{sur}/E_{crit} are equal to 6.7, 3.2 and 0.8 for shot #1050017, shot #1050021 and #1050019, respectively.

rate of $-30/s$. It is difficult to observe significant growth of RE current even with the large positive toroidal electric field in figure 6, which is similar to previous observations in JT-60U experiments [49].

4. HXR bremsstrahlung spectrum analysis

4.1. Comparison of HXR bremsstrahlung spectrum with different E_{sur}/E_{crit}

The typical HXR bremsstrahlung spectra of the lost REs from the MCA are shown in figure 7. To describe the HXR emission evolution clearly, we define the following two characteristic parameters:

- The maximum energy $\max E_{RE}$ is defined as the intersection of the log-linear fit of an HXR high-energy tail with the level $\log_{10} N_{\gamma}/s = 2$. The analysis method refers to [24].
- The HXR temperature T_{HXR} is derived from the log-linear fit of an HXR high-energy tail, $T_{HXR} = -1/k$, where k is the slope of the fitting line. The analysis method refers to [50, 51]. The T_{HXR} can represent the energy of the HXR spectrum to a certain extent. The larger the T_{HXR} , the higher the HXR emission energy. The smaller the T_{HXR} , the lower the HXR emission energy.

HXR bremsstrahlung spectra from three discharges have the same pre-disruption plasma parameters but the different externally applied toroidal electric fields during the RE plateau phase. The HXR bremsstrahlung spectra shown in figure 7(a) are measured with the Forward HXR detector and (b) with the Backward HXR detector. The pitch angle of RE, $\theta = \arctan(v_{\perp}/v_{\parallel})$, where v_{\perp} is the velocity vector parallel to the magnetic field and v_{\parallel} is the perpendicular component. As shown in figure 1, the collimation chord of the Forward HXR

detector is aligned with the direction of REs movement, measuring small pitch-angle lost REs, and the collimation chord of the Backward HXR detector is opposite to the direction of REs movement, measuring large pitch-angle lost REs. However, none of the HXR detectors in J-TEXT are absolutely calibrated. REs cannot be fully characterized by HXR emissions. The temperature of measured HXR spectra is not completely equal to the temperature of REs in the vacuum vessel. At present, we can only qualitatively describe the possible evolution trend of REs. In future work, we will do more calibration on the response of HXR detectors.

The measurement time of the HXR bremsstrahlung spectra is a period during the RE plateau phase when the evolution of RE current is stable, usually 15 ms after MGI injection until the beginning of the RE CQ. Three discharges shown in figure 7 are in the different conditions of E_{sur}/E_{crit} which are equal to 6.7, 3.2 and 0.8.

It can be seen clearly that with E_{sur}/E_{crit} increasing, the T_{HXR} from Forward HXR detector decreases but the T_{HXR} from the Backward HXR detector increases, which means the large pitch-angle lost REs become more energetic but the small pitch-angle lost REs become less energetic. The defined maximum energy $\max E_{RE}$ is similar to the variation of T_{HXR} . The temporal evolution of the HXR spectrum and the detailed analysis are described in the next section.

4.2. Temporal evolutions of HXR spectrum with different electric fields

The temporal evolutions of HXR emissions during disruptions with different electric fields are shown in figure 8. The HXR spectrum is shown for every 1.5 ms and obtains the two characteristic parameters mentioned above as well as the flux and total counts rate of HXR emissions. Figure 8 shows the temporal evolutions of these four characteristic parameters in two discharges. Setting $V_{loop} \sim 10$ V, $E_{sur}/E_{crit} = 6.7$ in shot

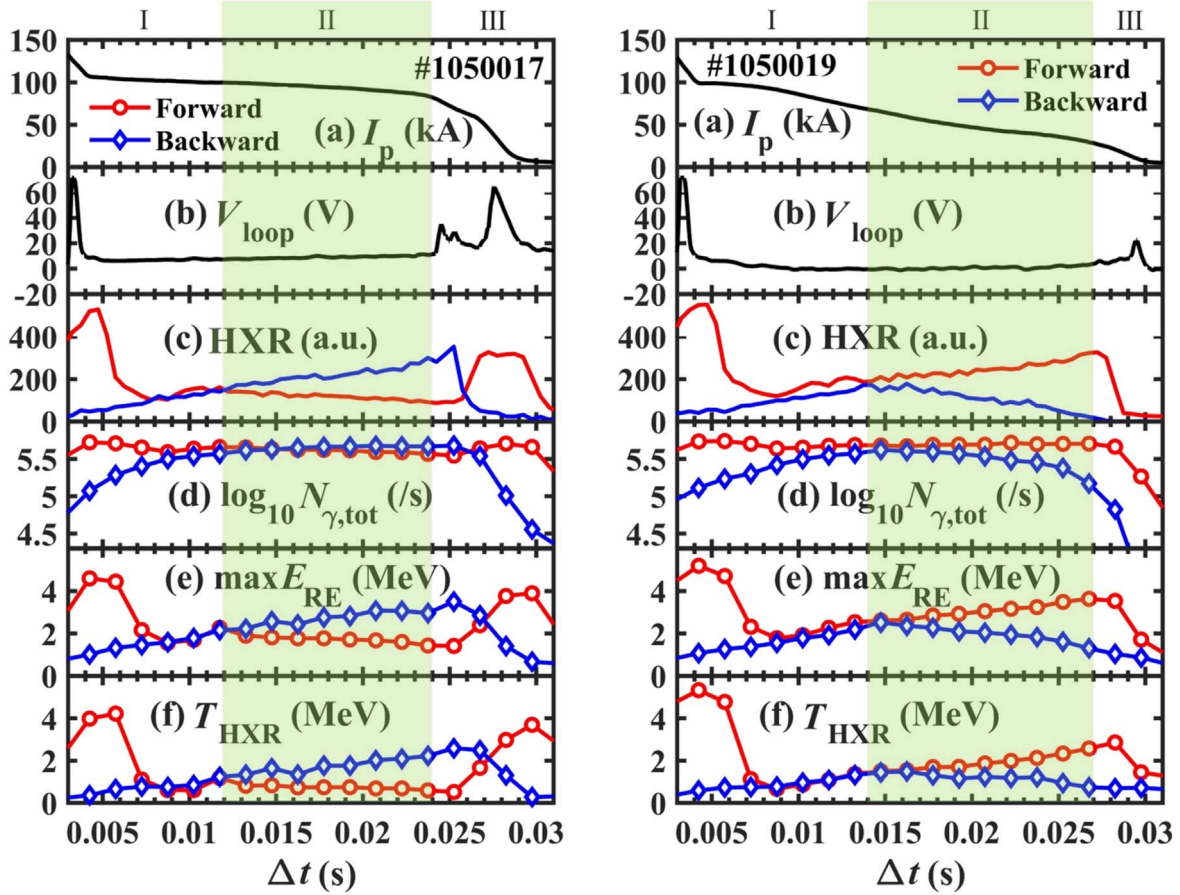


Figure 8. Time traces from two discharges differing primarily in the externally applied toroidal electric field direction during disruption showing (a) plasma current I_p , (b) toroidal loop voltage V_{loop} , (c) HXR flux, (d) total counts rate $\log_{10} N_{\gamma, tot}$, (e) defined maximum energy $\max E_{RE}$, (f) HXR temperature T_{HXR} . Data of HXR bremsstrahlung spectra represented by red lines and blue lines are from Forward HXR detector and Backward HXR detector. E_{sur}/E_{crit} are equal to 6.7 and 0.8 in shot #1050017 and shot #1050019, respectively. The MGI trigger time is at $T_{MGI} = 0.3$ s and $\Delta t = t - T_{MGI}$.

#1050017 and $V_{loop} \sim 0$ V, $E_{sur}/E_{crit} = 0.8$ in shot #1050019.

The disruption is divided into three phases to analyze the temporal evolution of the HXR spectrum. There are two division criteria for the second phase. First, select the time range where toroidal loop voltage varies relatively slowly without obvious spikes. Second, select the time range where the temporal evolution of HXR emission approximately linear. For the two discharges in figure 7, first, the initial phase is defined as the middle of CQ to the initial phase of RE plateau (marked by I in figure 8), corresponding to the 0.003–0.012 s in shot #1050017 and 0.003–0.014 s in shot #1050019. Second, the middle phase is defined as the middle phase of the RE plateau (marked by II in figure 8), corresponding to the 0.012–0.024 s in shot #1050017 and 0.014–0.027 s in shot #1050019. Third, the RE CQ phase (marked by III in figure 8), corresponding to the 0.024–0.031 s in shot #1050017 and 0.027–0.031 s in shot #1050019.

4.2.1. The initial phase. For different applied toroidal electric fields, the temporal evolution trend of each characteristic parameter is similar. For the forward HXR emission, the

$\log_{10} N_{\gamma, tot}$ and the T_{HXR} rise rapidly. A large number of REs are generated and accelerated due to the large toroidal loop voltage during CQ. At the same time, a large fraction of REs are lost from the RE beam. The drop of the forward $\log_{10} N_{\gamma, tot}$ and the forward T_{HXR} can be seen during the RE current initial formation phase, which probably due to the better confinement of REs.

As for the backward HXR emission, the temporal evolution of it is simple. The backward $\log_{10} N_{\gamma, tot}$ and the backward T_{HXR} both keep slowly rising during the initial phase, and their values are lower than those of the forward. It seems that the loss of REs during the initial phase is dominated by the small pitch-angle REs rather than the large pitch-angle REs.

4.2.2. The middle phase. Compared with the initial phase, the evolution trend of HXR emission in the middle phase is gentler but performs a different evolution trend with different toroidal electric fields. In shot #1050017 with higher E_{sur}/E_{crit} , the forward T_{HXR} decays but the backward T_{HXR} grows. In shot #1050019 with lower E_{sur}/E_{crit} , the evolution trend of HXR emission is opposite to the shot with higher

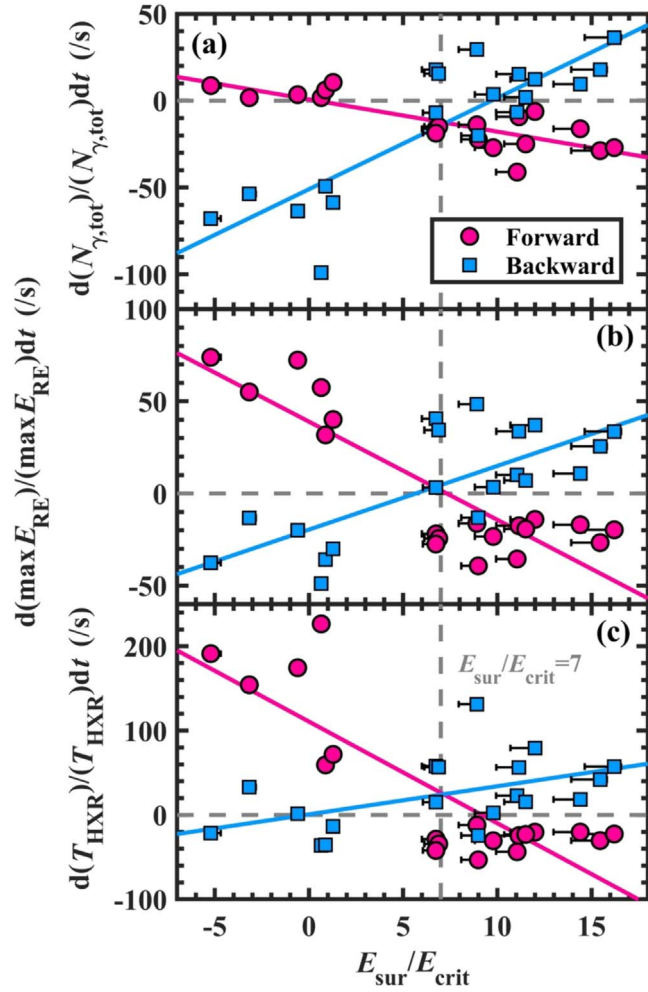


Figure 9. Comparison of the growth rate of (a) total counts rate $\log_{10}N_{\gamma,\text{tot}}$, (b) defined maximum energy $\max E_{\text{RE}}$ and (c) HXR temperature T_{HXR} from the Forward HXR detector and the Backward HXR detector versus the ratio of surface electric field and critical electric field $E_{\text{sur}}/E_{\text{crit}}$.

$E_{\text{sur}}/E_{\text{crit}}$: the forward T_{HXR} grows but the backward T_{HXR} decays. The evolution trend of the $\log_{10}N_{\gamma,\text{tot}}$ is similar to the T_{HXR} in the two discharges. During this phase, HXR emission seems to be mainly affected by the toroidal electric field. As mentioned in section 2.2, the Forward HXR detector measures small pitch-angle lost REs and the Backward HXR detector measures large pitch-angle lost REs. These observations may indicate: when a higher $E_{\text{sur}}/E_{\text{crit}}$ is applied (shot #1050017), large pitch-angle lost REs become more energetic, and small pitch-angle lost REs become less energetic. In the case of the lower $E_{\text{sur}}/E_{\text{crit}}$ applied (shot #1050019), it is opposite that large pitch-angle lost REs become less energetic and small pitch-angle lost REs become more energetic. Detailed statistical results during this phase are given in figure 9.

4.2.3. The RE CQ phase. In shot #1050017 with higher $E_{\text{sur}}/E_{\text{crit}}$, the variation of the plasma current is quite large during RE CQ phase so a large toroidal loop voltage is

induced. It can be obviously seen that the forward HXR emissions lag behind the backward. During the first reduction phase of RE current which is corresponding to the first spike of toroidal loop voltage, what can be clearly seen that the drop of backward T_{HXR} and $\log_{10}N_{\gamma,\text{tot}}$ is mainly caused by the loss of large pitch-angle REs. The increase of forward T_{HXR} and $\log_{10}N_{\gamma,\text{tot}}$ reflect the acceleration of small pitch-angle REs caused by the large toroidal loop voltage. During the second reduction phase of RE current which is corresponding to the second spike of toroidal loop voltage, the RE beam completely loses displacement control and directly hits the vacuum vessel wall, where the final drop of forward T_{HXR} and $\log_{10}N_{\gamma,\text{tot}}$ can be seen.

In shot #1050019 with lower $E_{\text{sur}}/E_{\text{crit}}$, the variation of the plasma current and the induced toroidal loop voltage are both small during RE CQ phase. There are only a small fraction of large pitch-angle REs losses. Without large toroidal loop voltage, the REs will almost not be accelerated so that there is no obvious rise in the forward T_{HXR} and $\log_{10}N_{\gamma,\text{tot}}$. The evolution trend of HXR flux and the $\max E_{\text{RE}}$ is similar to the T_{HXR} during the whole disruption phase.

4.3. Characteristics of HXR

It seems that characteristic parameters in the phases II and III have a high correlation with the toroidal electric field. Figure 9 shows the growth rate of the total counts rate $\log_{10}N_{\gamma,\text{tot}}$, the defined maximum energy $\max E_{\text{RE}}$ and the photon temperature T_{HXR} in forward and backward directions versus the ratio of surface electric field and critical electric field $E_{\text{sur}}/E_{\text{crit}}$, respectively. The time range of characteristic parameters in each discharge plotted in figure 9 is during the phase II, i.e. the middle phase of RE plateau mentioned above, when the influence of MGI gas injection is negligible and there is no obvious fluctuation in toroidal loop voltage. Each circle or square pair in figure 9 corresponds to the middle phase of the RE plateau in a single discharge. The horizontal error bars in figure 9 reflect the range in E_{crit} obtained from the error bar of Z_{mean} (the same in figure 6).

As the $E_{\text{sur}}/E_{\text{crit}}$ increases, the growth rates of forward characteristic parameters are increasing, and the growth rates of backward characteristic parameters are decreasing. These statistical results may mean that as the $E_{\text{sur}}/E_{\text{crit}}$ increases, the energy and quantity of small pitch-angle lost REs decrease, while the energy and quantity of large pitch-angle lost REs increase. The possible reasons for these observations will be discussed in section 5. Furthermore, the fitting line of the growth rate of each characteristic parameter from forward or backward direction has the same intersection at $E_{\text{sur}}/E_{\text{crit}} \sim 7$. The transition from growth to decay is found to occur 3–5 times above the theoretical critical electric field measured by HXR emission under quiescent conditions in DIII-D [28]. On the other hand, the transition of the RE current from growth to decay (or from decay to growth) happens at $E_{\text{sur}}/E_{\text{crit}} \sim 12$ in J-TEXT which is shown in figure 7. In response to changes in the toroidal electric field, there is a $\sim 5 \times E_{\text{sur}}/E_{\text{crit}}$ difference between the growth rate of the RE current and the lost REs.

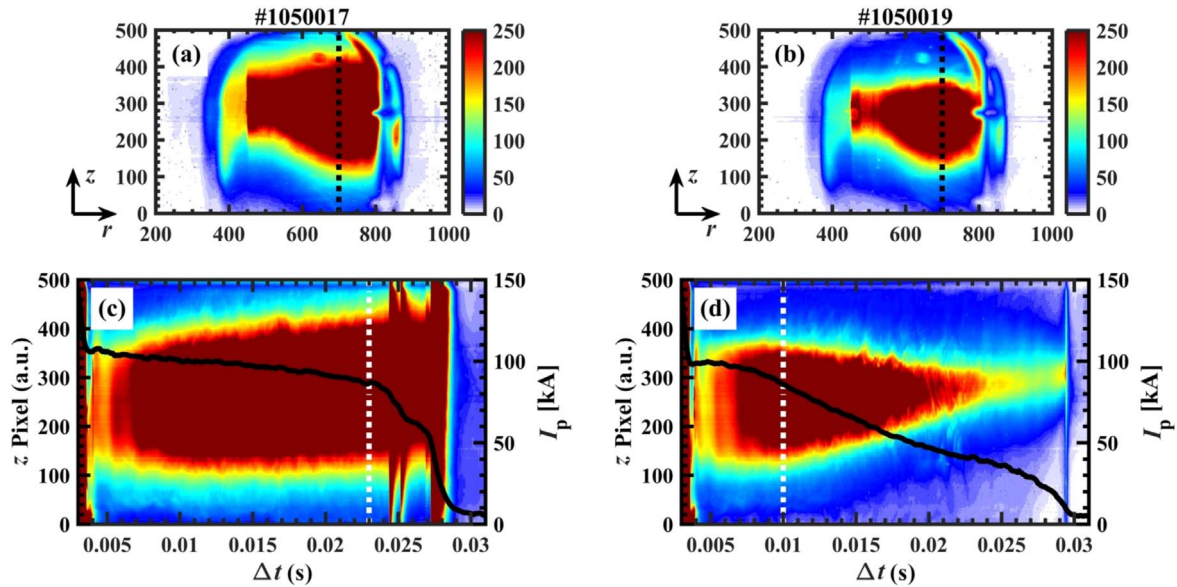


Figure 10. Ar II (442 nm) emissions measured with a filtered fast frame visible camera during disruptions in two discharges: $E_{\text{sur}}/E_{\text{crit}}$ are equal to 6.7 and 0.8 in shot #1050017 and shot #1050019, respectively. Black dotted lines in (a) and (b) represent z -axis pixel at $r = 700$, whose temporal evolution is drawn in (c) and (d) for the two discharges. The Ar II emission profiles are plotted in (a) and (b) at the moment when the plasma current I_p of two discharges is the same, which is represented by white dotted lines in (c) and (d). Black solid lines in (c) and (d) represent the temporal evolutions of the plasma current I_p . The MGI trigger time is at $T_{\text{MGI}} = 0.3$ s and $\Delta t = t - T_{\text{MGI}}$.

The influence of the toroidal electric field on the energy and the number of REs at different pitch angles is different. When $E_{\text{sur}}/E_{\text{crit}} < 1$, the forward $\max E_{\text{RE}}$ and T_{HXR} growth rate are abnormally large, while the forward $\log_{10} N_{\gamma, \text{tot}}$ growth rate is small. That means when a large negative toroidal electric field is applied, forward HXR emissions are enhanced mainly due to the acceleration of small pitch-angle lost REs rather than an increase in the number of them. The backward $\max E_{\text{RE}}$ and T_{HXR} growth rate drop a little, while the backward $\log_{10} N_{\gamma, \text{tot}}$ growth rate drops a lot. The backward HXR emissions are reduced mainly due to the decrease in the number of large pitch-angle lost REs rather than the deceleration of them.

When $E_{\text{sur}}/E_{\text{crit}} > 7$, the values of the backward $\max E_{\text{RE}}$ and T_{HXR} growth rate can exceed than zero easily. However, it is difficult to observe a large rise in RE current growth rate during the RE plateau phase in figure 6.

5. Discussion

This work has indicated that the transition of REs from growth to decay occurs at 12 times above the theoretical critical electric field by measuring RE current and 7 times by measuring HXR emission. In response to the changes of $E_{\text{sur}}/E_{\text{crit}}$, the forward and backward HXR emissions show the opposite evolution trend. Possible sources are now discussed.

In order to study the effect on the argon impurities to REs, the fast frame visible camera with an Ar II (442.6 nm) filter is used to obtain the image which is expected to be dominated by line emission. The Ar II emission profiles in figures 10(a) and (b) are chosen at the time when the plasma

current is the same. The temporal evolutions of the z -axis pixel and the plasma current I_p are shown in figures 10(c) and (d).

Strong emissions of the RE beam during disruptions can be seen in the image. Before $\Delta t = 0.01$ s, the emission evolution trend is similar between the two discharges. Then the emission distribution becomes different after the externally toroidal loop voltage is applied at $\Delta t = 0.01$ s. In shot #1050017 with higher $E_{\text{sur}}/E_{\text{crit}}$, even though the plasma current is slightly reduced over time, the emission distribution is wider. During the RE CQ phase, there are several large bursts of the emission distribution at the moment that the plasma current changes rapidly. Previous research in [19] has found that the RE loss is related to kink instabilities with similar bursts observed in the magnetic probe and HXR signals. However, in shot #1050019 with lower $E_{\text{sur}}/E_{\text{crit}}$, as the plasma current decreases, the emission distribution becomes narrower and weaker.

The Ar II emission profile of the shot with higher $E_{\text{sur}}/E_{\text{crit}}$ is much broader than that of the shot with lower $E_{\text{sur}}/E_{\text{crit}}$ under the condition of the same plasma current. The previous result in figure 9 shows that when higher $E_{\text{sur}}/E_{\text{crit}}$ is applied, large pitch-angle lost REs are accelerated and increased. This Ar II emission profile may confirm the result of figure 9 that higher $E_{\text{sur}}/E_{\text{crit}}$ may enhance the radial transport of REs and may cause high-energy REs to be scattered to a larger pitch angle. Furthermore, it would appear that the large toroidal electric field enhances the ionization of argon. Simulation results in [52, 53] indicate that given the impact of collisions with screened nuclei on the dynamics of REs, RE beams will be strongly damped and the critical electric field will be increased due to the enhanced radiation loss rates in the presence of ionized impurities. This may

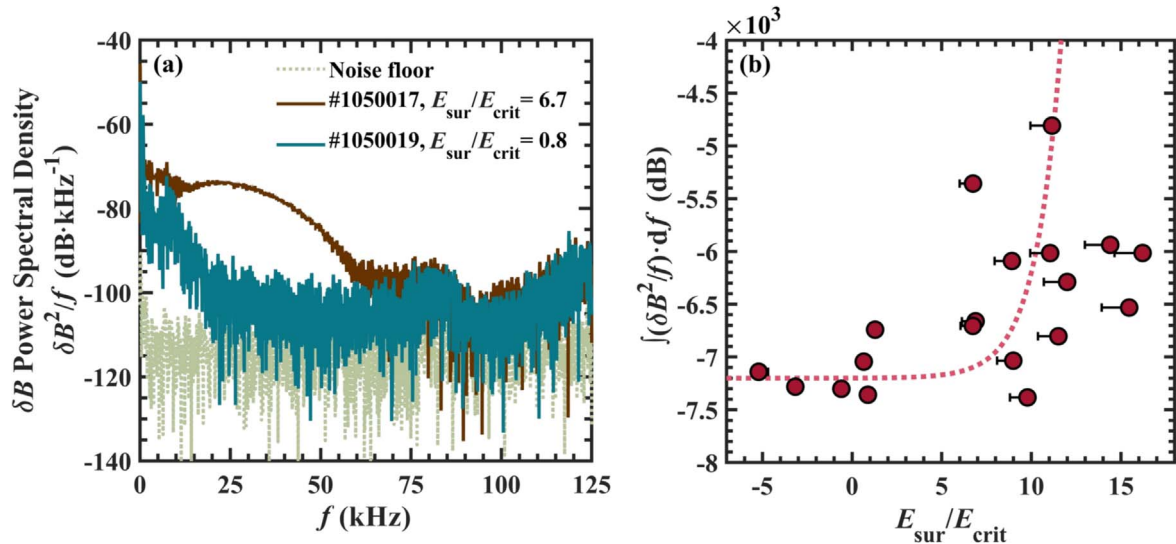


Figure 11. (a) Density-weighted magnetic fluctuation data are measured by Mirnov coil for discharges with different toroidal electric fields: $E_{\text{sur}}/E_{\text{crit}}$ are equal to 6.7 and 0.8 in shot #1050017 and shot #1050019, respectively. The noise floor is measured prior to discharge initiation. (b) Density-weighted magnetic fluctuation data integration from 0 to 125 kHz for the discharges which were shown in figure 9 versus the ratio of surface electric field and critical electric field, $E_{\text{sur}}/E_{\text{crit}}$. There seems to be an exponential relationship between the density-weighted magnetic fluctuation data integration and the $E_{\text{sur}}/E_{\text{crit}}$. The scarlet dotted line shows this possible relationship.

explain the result shown in figure 6: through the analysis of figure 10, it can be found that the ionization of argon may be enhanced by the larger applied toroidal loop voltage. When a larger toroidal loop voltage is applied, because the partially ionized impurities are heavier, it is difficult to observe an obvious increase of the RE current growth rate in figure 6. Furthermore, the critical electric field is also increased by about 10 times as mentioned before due to the presence of ionized argon impurities.

In addition, the Mirnov coil is used to estimate magnetic fluctuation (δB) levels inside the RE beam, which are presented in figure 11(a). The measurement time range of two discharges is the same: Δt from 0.014 to 0.024 s. In the shot #1050017 with higher $E_{\text{sur}}/E_{\text{crit}}$, the magnetic fluctuation level in the range of 0–60 kHz is much stronger than the shot #1050019 with lower $E_{\text{sur}}/E_{\text{crit}}$. Note that when the frequency range is higher than 60 kHz, the magnetic disturbance level between two discharges becomes less obvious. However, for other discharges, the frequency range with strong magnetic fluctuation amplitude is not necessarily in the range of 0–60 kHz. Density-weighted magnetic fluctuation data integration from 0 to 125 kHz (full frequency range) for each discharge versus the $E_{\text{sur}}/E_{\text{crit}}$ is shown in figure 11(b). The horizontal error bars in figure 11(b) reflect the range in E_{crit} obtained from the error bar of Z_{mean} (the same in figure 6).

Seemingly, the integration of density-weighted magnetic fluctuation data grows exponentially with $E_{\text{sur}}/E_{\text{crit}}$ increasing, which can be seen from the dotted line in figure 11(b). When $E_{\text{sur}}/E_{\text{crit}}$ exceeds about 7, the density-weighted magnetic fluctuation data integration grows rapidly. This is very consistent with the growth/decay transition of the HXR characteristic parameters at $E_{\text{sur}}/E_{\text{crit}} \sim 7$ in figure 9. Previous studies have shown that kinetic instabilities in the MHz range driven by REs are considered to be a possible way to

cause the losses of REs. Wave-particle interactions can increase the pitch-angle scattering of REs, therefore, they can induce local magnetic perturbations increasing the RE radial transport [24]. The kinetic whistler wave instabilities can give a strong pitch-angle scattering for REs in the simulation of [30]. Also, a radial diffusive loss of REs can occur due to magnetic fluctuations in the kHz range, which has been reported in [28]. The above researches all mean that the magnetic fluctuations possibly increase the RE radial transport and give a strong pitch-angle scattering for REs.

In figure 9, when a large $E_{\text{sur}}/E_{\text{crit}}$ is applied, the backward HXR emission is enhanced in energy and quantity of discharges (i.e. large pitch-angle lost REs are accelerated and increased), which might be caused by the enhanced magnetic fluctuation. There is a probability that the large toroidal electric field enhances magnetic fluctuation in the kHz range, leading to the enhance of radial losses of REs and thereby causing the increase of the pitch angle of lost REs. Previous studies in DIII-D have given a proposed mechanism for RE loss, which is very similar to our inferences: the decay of the plasma current during the CQ induces loop voltage, loop voltage accelerates REs, high-energy REs drive kinetic instabilities, instabilities increase the loss of REs [24].

It is not clear why the small pitch-angle lost REs become less energetic (showing a decline in forward HXR emission) when a higher toroidal electric field is applied. The whistler wave instabilities described in [21] can prevent REs from acceleration to high energies. The low-frequency magnetic fluctuations mentioned in figure 11 might also slow down the small pitch-angle RE. But it still cannot explain why these magnetic fluctuations have different effects on REs of different pitch angles. Future experiments will attempt to obtain the precise pitch angle of RE by some new diagnostics and deeply analyze the impact of instabilities on REs.

6. Summary

The soft landing of RE currents by ohmic field has been performed in J-TEXT tokamak. Under the condition that the RE beam position has been well controlled, the toroidal electric field has been scanned from 1.6 to -0.3 V m^{-1} during RE plateau phases, which is aimed to improve the understanding of RE generation. It is found that when the toroidal electric field is less than 7–12 times the theoretical critical electric field, the decay of REs may occur. When the surface toroidal electric field is less than about 0.6 V m^{-1} in J-TEXT, a significant ramp down of RE current can be achieved. The maximum RE current dissipation rate by the ohmic field is about 3 MA s^{-1} in J-TEXT. An anomalous REs dissipation rate of about $-30/\text{s}$ always exists compared with the avalanche theory. Because of this anomalous dissipation rate of REs, the HXR bremsstrahlung spectra have been analyzed: when the higher toroidal electric field is applied, the enhancement of backward HXR emission and the reduction of forward HXR emission are observed. When the lower toroidal electric field is applied, the enhancement of forward HXR emission and the reduction of backward HXR emission are observed.

In addition, some possible effects on the anomalous RE loss are observed in the experiments. The Ar II emission results suggest that the large toroidal electric field probably enhances the ionization of argon. Due to the impact of collisions with screened nuclei on the dynamics of REs [52, 53], the presence of partially ionized argon impurities then enhances radiation loss rates and increases the critical electric field. Also, the enhanced magnetic fluctuations affected by the large toroidal electric field may result in the enhancement of the RE radial losses and change the RE loss characteristics. These results indicate that when the different toroidal electric fields are applied, the physical process of RE generation and loss may be different.

The experimental results in J-TEXT show that the soft landing of RE current by ohmic field has a good effect on the dissipation of RE currents. Due to the parameters of J-TEXT tokamak are much lower than ITER, further experiments are required to perform in other medium or large-sized devices. In addition, the control of density and toroidal electric field can be combined to optimize the dissipation effect on RE currents. Further work needs to be carried out to appropriately combine this soft-landing strategy and MGI/SPI in RE dissipation experiments of J-TEXT.

Acknowledgments

This work is supported by the National Key R&D Program of China (No. 2017YFE0302000), the National Magnetic Confinement Fusion Science Program of China (Nos. 2015GB111002, 2015GB104000), National Natural Science Foundation of China (Nos. 11775089, 51821005, 71762031,

11575068 and 11905077) and the China Postdoctoral Science Foundation (2019M652615).

References

- [1] Dreicer H 1959 *Phys. Rev.* **115** 238
- [2] Smith H M and Verwichte E 2008 *Phys. Plasmas* **15** 072502
- [3] Savrukhin P V 2006 *Plasma Phys. Control. Fusion* **48** B201
- [4] Lehnen M et al 2011 *Nucl. Fusion* **51** 123010
- [5] Whyte D G et al 2003 *J. Nucl. Mater.* **313–316** 1239
- [6] Reux C et al 2010 *Nucl. Fusion* **50** 095006
- [7] Olynyk G M et al 2013 *Nucl. Fusion* **53** 092001
- [8] Wei Y N et al 2019 *Plasma Phys. Control. Fusion* **61** 084003
- [9] Reux C et al 2015 *Nucl. Fusion* **55** 129501
- [10] Li Y et al 2018 *Rev. Sci. Instrum.* **89** 10K116
- [11] Commaux N et al 2016 *Nucl. Fusion* **56** 046007
- [12] Rosenbluth M N and Putvinski S V 1997 *Nucl. Fusion* **37** 1355
- [13] Gobbin M et al 2018 *Plasma Phys. Control. Fusion* **60** 014036
- [14] Mlynar J et al 2019 *Plasma Phys. Control. Fusion* **61** 014010
- [15] Commaux N et al 2011 *Nucl. Fusion* **51** 103001
- [16] Lehnen M et al 2008 *Phys. Rev. Lett.* **100** 255003
- [17] Lin Z F et al 2019 *Plasma Phys. Control. Fusion* **61** 024005
- [18] Riccardo V et al 2010 *Plasma Phys. Control. Fusion* **52** 124018
- [19] Paz-Soldan C et al 2019 *Plasma Phys. Control. Fusion* **61** 054001
- [20] Liu Y Q et al 2019 *Nucl. Fusion* **59** 126021
- [21] Spong D A et al 2018 *Phys. Rev. Lett.* **120** 155002
- [22] Lvovskiy A et al 2019 *Nucl. Fusion* **59** 124004
- [23] Lvovskiy A et al 2020 *Nucl. Fusion* **60** 056008
- [24] Lvovskiy A et al 2018 *Plasma Phys. Control. Fusion* **60** 124003
- [25] Hollmann E M et al 2013 *Nucl. Fusion* **53** 083004
- [26] Wei Y N et al 2020 *Plasma Phys. Control. Fusion* **62** 025002
- [27] Shiraki D et al 2018 *Nucl. Fusion* **58** 056006
- [28] Paz-Soldan C et al 2014 *Phys. Plasmas* **21** 022514
- [29] Granetz R S et al 2014 *An Phys. Plasmas* **21** 072506
- [30] Liu C et al 2018 *Phys. Rev. Lett.* **120** 265001
- [31] Hollmann E M et al 2011 *Nucl. Fusion* **51** 103026
- [32] Liang Y et al 2019 *Nucl. Fusion* **59** 112016
- [33] Zeng L et al 2017 *Nucl. Fusion* **57** 046001
- [34] Ma T K et al 2017 *Nucl. Instrum. Methods Phys. Res. A* **856** 81
- [35] Chen Z Y et al 2008 *Plasma Phys. Control. Fusion* **50** 015001
- [36] Martín-Solís J R et al 2004 *Nucl. Fusion* **44** 974
- [37] Esposito B et al 2003 *Phys. Plasmas* **10** 2350
- [38] Fredrickson E D et al 2015 *Nucl. Fusion* **55** 013006
- [39] Eidietis N W et al 2012 *Phys. Plasmas* **19** 056109
- [40] Boncagni L et al 2013 *Fusion Eng. Des.* **88** 1109
- [41] Carnevale D et al 2019 *Plasma Phys. Control. Fusion* **61** 014036
- [42] Ficker O et al 2019 *Nucl. Fusion* **59** 096036
- [43] Loarte A et al 2011 *Nucl. Fusion* **51** 073004
- [44] Dai A J et al 2018 *Plasma Phys. Control. Fusion* **60** 055003
- [45] Pautasso G et al 2015 *Nucl. Fusion* **55** 033015
- [46] Wesson J et al 2011 *Tokamaks* 4th edn (Oxford: Oxford University Press)
- [47] Spitzer L Jr and Härm R 1953 *Phys. Rev.* **89** 977
- [48] Zhang X L et al 2019 *Fusion Eng. Des.* **147** 111241
- [49] Yoshino R and Tokuda S 2000 *Nucl. Fusion* **40** 1293
- [50] Younis J et al 2008 *Plasma Sci. Technol.* **10** 529
- [51] Younis J et al 2009 *Plasma Phys. Control. Fusion* **51** 075017
- [52] Hesslow L et al 2017 *Phys. Rev. Lett.* **118** 255001
- [53] Hesslow L et al 2018 *Plasma Phys. Control. Fusion* **60** 074010